Chinese Journal of
POLYMER SCIENCE

RESEARCH ARTICLE

https://doi.org/10.1007/s10118-026-3810-7
Chinese J. Polym. Sci.

Regulating Intermolecular Interactions through Phenyl-alkyl Side-chain Engineering for High-efficiency Organic Solar Cells

Yang Yi[a], Shen-Bo Zhu[a], Ming-Hao Jin[a], Jia-Yin Lyu[a], Zhi-Bo Wang[a], Rui-Han Li[a], Xiao-Nan Xu[a], Xue-Chen Jiao[b], and Hua-Wei Hu[a*]

[a] *State Key Laboratory of Advanced Fiber Materials, College of Materials Science and Engineering, Donghua University, Shanghai 201620, China*
[b] *National Synchrotron Radiation Laboratory, University of Science and Technology of China, Hefei 230029, China*

Electronic Supplementary Information

Abstract Regulating donor–acceptor (D/A) and acceptor–acceptor (A/A) interactions is crucial for optimizing the morphology and charge dynamics of organic solar cells (OSCs). Herein, a tetraphenylethylene (TPE)-containing Y-series acceptor, TPE-HD, was developed through phenyl-alkyl side-chain engineering to manipulate the intermolecular interactions and crystallization behavior. The introduced TPE unit enhanced A/A self-aggregation and molecular ordering, leading to increased crystallinity and accelerated crystallization kinetics during film formation. The binary D18:TPE-HD blend exhibited pronounced aggregation characteristics and delivered a power conversion efficiency (PCE) of 17.5%. To further exploit the favorable packing characteristics of TPE-HD, it was incorporated as a third component into the D18:L8-BO host system. Benefiting from the synergistic effects of the efficient exciton dissociation provided by L8-BO and the enhanced electron transport induced by TPE-HD, the ternary blend exhibited optimized phase separation, improved charge transport, and suppressed recombination. Consequently, the ternary OSC achieved a PCE of 19.8% with simultaneous improvements in the short-circuit current density, fill factor, and open-circuit voltage. This work demonstrates an effective strategy for regulating intermolecular interactions through phenyl–alkyl side-chain engineering to synergistically optimize the morphology and charge dynamics of high-performance OSCs.

Keywords Organic solar cells; Side-chain engineering; Intermolecular interaction; Morphology; Crystallization kinetics

Citation: Yi, Y.; Zhu, S. B.; Jin, M. H.; Lyu, J. Y.; Wang, Z. B.; Li, R. H.; Xu, X. N.; Jiao, X. C.; Hu, H. W. Regulating intermolecular interactions through phenyl-alkyl side-chain engineering for high-efficiency organic solar cells. *Chinese J. Polym. Sci.* https://doi.org/10.1007/s10118-026-3810-7

INTRODUCTION

Organic solar cells (OSCs) have broad application prospects in building-integrated photovoltaics, indoor photovoltaic systems, and wearable electronic devices owing to their advantages, such as light weight, good flexibility, semitransparency, and tunable color.[1–6] With the continuous optimization of non-fullerene acceptors (NFAs) in molecular design and device fabrication, the power conversion efficiency (PCE) of single-junction OSCs has recently exceeded 20%, demonstrating their strong potential for practical applications.[7–14] Further improvement of the OSC performance relies on the regulation of the nanoscale morphology in the bulk heterojunction active layer. However, achieving an appropriate phase separation size and balanced crystallinity remains a core challenge.[15–17] Specifically, excessive phase separation and crystallinity reduce the donor–acceptor interface area, which is detrimental to exciton dissociation; conversely, insufficient phase separation and crystallinity exacerbate carrier recombination, hindering charge transport.[18–20]Among various molecular engineering strategies, side-chain modification of A-DA′D-A-type acceptors has proven particularly effective in regulating intermolecular interactions and aggregation behavior.[21–23] Currently, two main side-chain structures are employed. The first strategy involved the use of a bulky phenyl group.[24–26] The steric hindrance introduced by the phenyl ring effectively suppresses excessive molecular aggregation, prevents the formation of overly large phase-separation domains, and maintains a favorable donor–acceptor interface, thereby optimizing the active layer morphology for exciton dissociation. However, this steric hindrance often leads to an increased π-π stacking distance and reduced crystallinity, which are unfavorable for carrier mobility. Consequently, devices based solely on such bulky side chains typically exhibit compromised charge transport and low fill factors. The second strategy involves the use of long alkyl side chains.[27–29] These chains enhance molecular solubility, promote ordered packing, and improve both crystallinity and carrier mobility. Nevertheless, the strong aggregation tendency induced by the long alkyl chains often leads to the formation of large pure-phase aggregates. Such oversized pure-phase domains reduce the donor–acceptor interfacial area, thereby exac-

* Corresponding author, E-mail: huaweihu@dhu.edu.cn
Invited Research Article
Received May 29, 2026; Accepted July 9, 2026; Published online August 27, 2026

erbating monomolecular recombination in the donor or acceptor pure phases and lowering exciton dissociation efficiency. To address this trade-off, an alkyl chain strategy based on a phenyl group has been proposed:[30–32] integrating a phenyl moiety into the alkyl side chain combines the steric hindrance effect of the phenyl group with the solution processability and ordered packing promotion ability of the alkyl chains. This design is expected to achieve an optimal active layer morphology, balance domain size, molecular packing, and charge transport properties, and holds great potential for further improving the performance of organic solar cells.

In this work, we designed and synthesized a tetraphenylethylene (TPE)-functionalized Y-series acceptor (TPE-HD) derived from L8-BO to systematically tune the balance between donor and acceptor (D/A) and acceptor–acceptor (A/A) interactions. The incorporation of TPE units strengthens the A/A interactions and promotes molecular ordering, leading to enhanced crystallization kinetics and increased crystallinity during film formation. The binary D18:TPE-HD blend exhibited strong self-aggregation, leading to an enlarged phase separation and limited exciton dissociation, resulting in a PCE of 17.5%. To further exploit its packing characteristics, TPE-HD was introduced as a third component into the D18:L8-BO host system. In the ternary system, L8-BO ensures efficient exciton generation and favorable donor–acceptor interfaces, whereas TPE-HD promotes ordered molecular packing and enhances electron transport, enabling a more balanced morphology. Consequently, the ternary device achieved an improved PCE of 19.8%, with improved short-circuit current density (J_{SC}), open-circuit voltage (V_{OC}), and fill factor (FF). This work provides a new perspective for tuning the balance of intermolecular interactions *via* side-chain engineering and demonstrates a promising ternary strategy for fabricating high-performance organic solar cells with synergistically optimized morphologies and charge dynamics.

EXPERIMENTAL

The synthetic details, experimental section and complementary data are presented in the electronic supplementary information (ESI).

RESULTS AND DISCUSSION

Materials Synthesis and Characterization

The chemical structure of TPE-HD is shown in Fig. 1(a), and the detailed synthetic procedure is provided in Scheme S1 (in ESI). The key DA'D intermediate was directly constructed from compound 1, followed by formylation and Knoevenagel condensation with 2-(5,6-difluoro-3-oxo-2,3-dihydro-1*H*-inden-1-ylidene)-malononitrile (2F-IC) to obtain the target acceptor material, TPE-HD. This material exhibits good solubility in common organic solvents, such as dichloromethane and chloroform, which is favorable for solution-processed device fabrication.

The optical properties of TPE-HD and L8-BO were investigated using UV-Vis absorption spectroscopy. As shown in Figs. 1(b) and 1(c), TPE-HD displays a maximum absorption peak at 731 nm in dilute solution, nearly identical to that of L8-BO, suggesting that introducing the TPE unit through the side chain exerts a negligible influence on the intrinsic conjugated backbone electronic structure. Upon film formation, both acceptors exhibited red-shifted absorption relative to their solution spectra because of the enhanced intermolecular interactions in the solid state. Notably, TPE-HD showed a smaller red-shift than L8-BO, accompanied by a reduced 0-0/0-1 vibronic peak ratio, indicative of reduced *J*-aggregation induced by the side-chain TPE unit.[33,34] The optical bandgaps of L8-BO and TPE-HD are estimated to be 1.44 and 1.42 eV, respectively. To further evaluate the electronic structure, cyclic voltammetry (CV) measurements were performed (Fig. 1d and Fig. S1 in ESI) to investigate the highest occupied molecular orbital (HOMO) and lowest unoccupied molecular

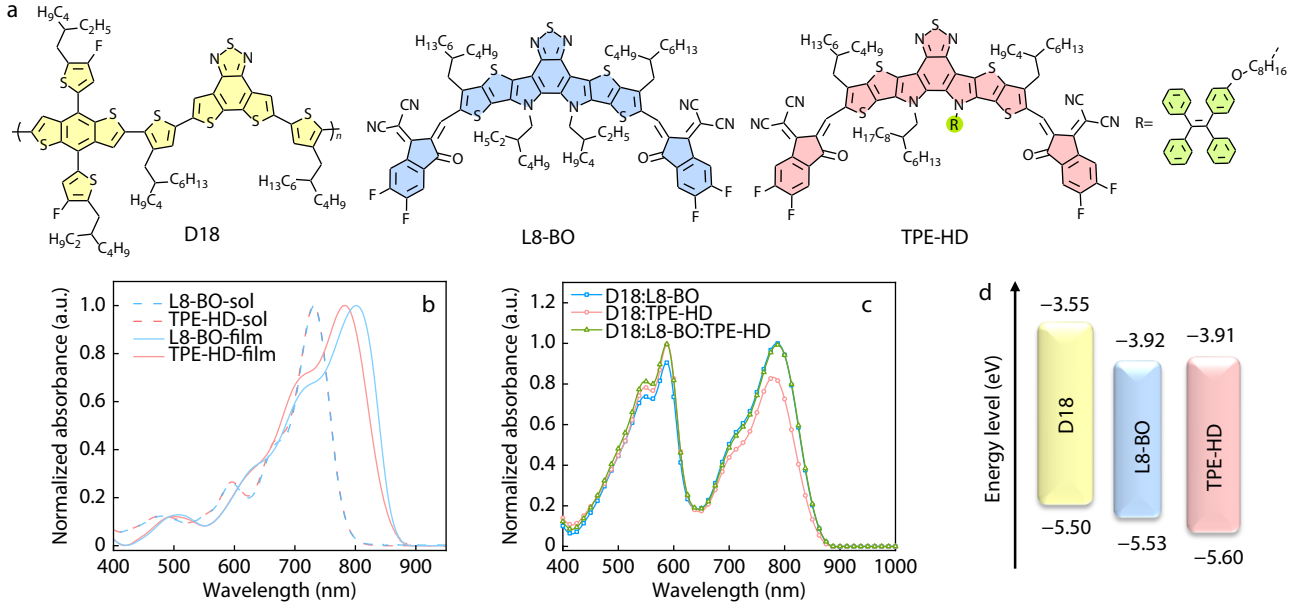

Fig. 1 (a) Chemical structures of D18, L8-BO, and TPE-HD; (b) Normalized UV-Vis absorption spectra in solution and neat film; (c) UV-Vis absorption spectra of the blend films; (d) The energy level diagrams of D18, L8-BO and TPE-HD.

orbital (LUMO) energy levels. As summarized in Table S1 (in ESI), the HOMO/LUMO levels of D18, L8-BO, and TPE-HD were estimated to be −5.50/−3.55 eV, −5.53/−3.92 eV, and −5.60/−3.91 eV, respectively. Furthermore, the theoretically calculated LUMO/HOMO levels of L8-BO and TPE-HD were −3.53/−5.56 eV and −3.57/−5.60 eV (Fig. S2 in ESI), respectively. The results indicate that the incorporation of the TPE-functionalized side chain induced negligible changes in the frontier molecular orbital energy levels.

Photovoltaic Performance

The OSC devices were fabricated with a conventional ITO/2-PACz/active layer/PDINN/Ag structure, and the detailed fabrication and characterization procedures are provided in ESI. The current density-voltage curves of the optimized devices under AM 1.5G illumination are presented in Fig. 2(a), and the corresponding photovoltaic parameters are summarized in Table 1. The photovoltaic performances of the devices with different D/A ratios are shown in Fig. S3 and Table S2 (in ESI). The binary device based on D18:TPE-HD achieved a PCE of 17.5%, which was slightly lower than that of D18:L8-BO (18.8%). Nevertheless, V_{OC} increased from 0.894 V to 0.908 V, suggesting that the incorporation of TPE-HD effectively reduced the voltage loss. On this basis, when TPE-HD was added as a third component to the D18:L8-BO system, the resulting ternary device achieved an enhanced PCE of 19.8%, accompanied by simultaneously improved J_{SC}, FF, and V_{OC} of 27.3 mA·cm^{-2}, 80.4%, and 0.901 V, respectively. The corresponding EQE spectra are shown in Fig. 2(b). The integrated J_{SC} values for D18:L8-BO, D18:TPE-HD, and D18:L8-BO:TPE-HD-based devices are 26.1, 24.8, and 26.6 mA·cm^{-2}, respectively, which agree well with the *J-V* results, with deviations below 5%. The enhanced photovoltaic performance of the ternary device indicates that the introduction of TPE-HD contributes to more efficient photogenerated charge generation and collection.

To elucidate the origin of the V_{OC} differences, the energy loss components (ΔE_{loss}) of the devices were systematically analyzed, and the corresponding parameters are summarized in Fig. S4 and Table S3 (in ESI). Since the three systems exhibit nearly identical optical bandgaps, the radiative loss above the bandgap (ΔE_1) remains essentially unchanged among the devices. The D18:TPE-HD device delivered the lowest ΔE_{loss} of 0.551 eV, accompanied by the smallest non-radiative component (ΔE_3) of 0.228 eV. These results indicate

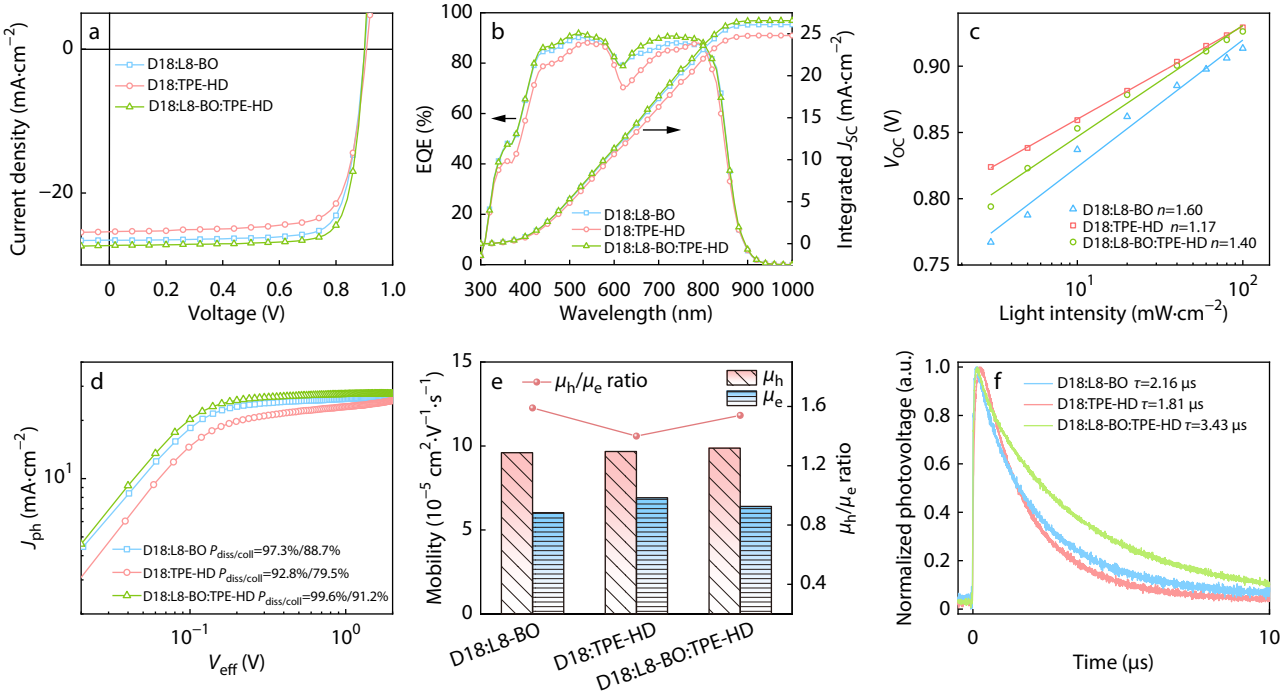

Fig. 2 (a) Current density-voltage (*J-V*) curves; (b) EQE spectra and integrated J_{SC} of corresponding devices; (c) V_{OC} versus light intensity curves; (d) J_{ph}-V_{eff} relationships curves; (e) Hole mobilities, electron mobilities, and μ_h/μ_e ratios based on D18:NFAs-based devices; (f) Transient photovoltage decay curves.

Table 1 Photovoltaic parameters of the D18:NFAs-based OSCs.

Active layer [a]	V_{OC} (V)	J_{SC} (mA·cm^{-2})	J_{SC}^{EQE} (mA·cm^{-2})	FF (%)	PCE (%)
D18:L8-BO	0.894 (0.893±0.002)	26.7 (26.3±0.4)	26.1	78.9 (78.5±0.4)	18.8 (18.6±0.3)
D18:TPE-HD	0.908 (0.907±0.002)	25.4 (25.0±0.4)	24.8	76.0 (75.6±0.4)	17.5 (17.2±0.3)
D18:L8-BO:TPE-HD	0.901 (0.898±0.003)	27.3 (26.9±0.4)	26.6	80.4 (80.0±0.4)	19.8 (19.5±0.3)

[a] The statistical results were obtained from at least 10 devices.

https://doi.org/10.1007/s10118-026-3810-7

that the incorporation of TPE-HD effectively suppressed non-radiative recombination, thereby reducing energy loss and enhancing V_{OC}.

Charge Transport, Extraction, and Recombination

To further understand the charge recombination behavior, the light-intensity dependence (P_{light}) of the photocurrent was investigated. As shown in Fig. S5 (in ESI), the α values are 0.92 for the D18:L8-BO, 0.94 for D18:TPE-HD, and 0.94 for the D18:L8-BO:TPE-HD-based ternary devices, respectively. Compared with D18:L8-BO, the binary and ternary devices containing TPE-HD had α values closer to 1, indicating that bimolecular recombination was effectively suppressed.[35,36] Furthermore, the voltage dependence on light intensity (Fig. 2c) shows that the slope factors (n) of the above devices are 1.60 (D18:L8-BO), 1.17 (D18:TPE-HD), and 1.40 (D18:L8-BO:TPE-HD), respectively, confirming that the introduction of TPE-HD effectively suppresses trap-assisted recombination. The charge generation and collection processes were further evaluated by measuring the photocurrent density (J_{ph}) as a function of effective voltage (V_{eff}), as shown in Fig. 2(d). The calculated exciton dissociation probability (P_{diss}) and charge collection efficiency (P_{coll}) for D18:L8-BO, D18:TPE-HD, and the ternary device are 97.3%/88.7%, 92.8%/79.5%, and 99.6%/91.2%, respectively. Compared to their binary counterparts, the ternary device exhibited the highest P_{diss} and P_{coll} values, demonstrating more efficient exciton dissociation and carrier collection, which contributed to the simultaneous enhancement of J_{SC} and FF.

The charge transport characteristics of the blend films were studied using the space-charge limited current (SCLC) method; detailed data are shown in Fig. 2(e) and Table S4 (in ESI). The hole and electron mobilities of the D18:L8-BO, D18:TPE-HD, and D18:L8-BO:TPE-HD blend films were $9.60\times10^{-5}/6.03\times10^{-5}$, $9.67\times10^{-5}/6.92\times10^{-5}$, and $9.87\times10^{-5}/6.40\times10^{-5}$ $cm^2\cdot V^{-1}\cdot s^{-1}$, corresponding to μ_h/μ_e ratios of 1.59, 1.40, and 1.54, respectively. The three blend films showed similar hole mobilities, whereas the electron mobility increased after introducing TPE-HD, accompanied by an improved carrier balance. Transient photocurrent (TPC) and transient photovoltage (TPV) measurements were subsequently performed to probe the carrier extraction and recombination dynamics. As shown in Fig. 2(f) and Fig. S6 (in ESI), the charge extraction times of the three devices are 0.13, 0.16, and 0.13 μs, respectively, and the corresponding carrier lifetimes are 2.16, 1.81, and 3.43 μs. The ternary device simultaneously exhibited the fastest charge extraction and the longest carrier lifetime, indicating more efficient carrier transport and suppressed recombination loss, thereby supporting the superior J_{SC} and FF of the ternary OSCs.

Intermolecular Interaction Analysis

The improvement in device performance is closely related to the regulation of intermolecular interactions.[37–39] To clarify the influence of the TPE unit on the phase separation behavior of the donor and acceptor materials, the donor/acceptor (D/A) interaction strength was first evaluated using the Flory-Huggins interaction parameter (χ), and the detailed results are summarized in Fig. S7 and Table S5 (in ESI). The surface energies (γ) of D18, L8-BO, and TPE-HD were measured to be 24.06, 30.24, and 33.12 $mJ\cdot m^{-2}$, respectively. Based on the formula $\chi \propto (\sqrt{\gamma_A}-\sqrt{\gamma_B})^2$, $\chi^{D18:TPE\text{-}HD}$ (0.72) > $\chi^{D18:L8\text{-}BO}$ (0.35) was obtained, indicating that D18 and TPE-HD have poor miscibility and weaker D/A interactions than D18/L8-BO.[40] Such reduced donor–acceptor interactions are expected to suppress excessive D/A mixing and facilitate optimized phase separation. To verify this result further, density functional theory (DFT) calculations were performed to assess intermolecular interaction characteristics. Conformational scans of the L8-BO and TPE-HD dimers were performed at the B3LYP-D3(BJ)/6-31G(d,p) level to obtain optimized geometries and electrostatic potential (ESP) distributions. As shown in Fig. 3(a), compared with L8-BO, the strong electron-donating group TPE in TPE-HD lowers its surface electrostatic potential, thereby weakening the D/A interaction and suppressing donor–acceptor mixing, which is consistent with the contact angle measurement trend.

The effect of the TPE unit on the A/A interactions was subsequently investigated using an independent gradient model based on Hirshfeld partition (IGMH) analysis.[41,42] As shown in Figs. 3(b) and 3(c), the blue regions represent significant attractive noncovalent interactions, red regions indicate repulsive interactions, and green regions correspond to van der Waals interactions. The results showed that both acceptor materials were dominated by weak noncovalent interactions, mainly van der Waals forces. More importantly, we also observed that the TPE groups underwent tight packing with the backbone structure, leading to stronger and more extensive intermolecular interactions and a higher A/A self-aggregation tendency for TPE-HD. In addition, the corresponding basis set superposition error (BSSE)-corrected interaction energy (E_{inter}) of the TPE-HD dimer is −61.6 kcal/mol, significantly stronger than that of the L8-BO dimer (−44.3 kcal/mol), confirming the strengthened A/A interaction induced by the TPE-functionalized side chain.

Morphology Analysis and Film Formation Kinetics

To further elucidate how the altered intermolecular interactions influence device performance, the bulk heterojunction morphology and film formation behavior of the blend films were systematically investigated. We first investigated the surface morphology of the three blend films using atomic force microscopy (AFM). As shown in Fig. S8 (in ESI), the D18:L8-BO, D18:TPE-HD, and D18:L8-BO:TPE-HD blend films exhibited different nanoscale morphological features, with root-mean-square roughness (R_q) values of 1.68, 2.51, and 1.59 nm, respectively. The TPE-HD binary blend film showed significantly large aggregates and pronounced phase separation. In contrast, the ternary blend film had a more uniform and smoother surface, forming a finely continuous interpenetrating fibrillar network structure, which was also verified by its phase image. This is beneficial for improving the exciton dissociation efficiency and constructing efficient charge transport pathways.

Furthermore, grazing-incidence wide-angle X-ray scattering (GIWAXS) was performed. The two-dimensional GIWAXS patterns of the films are shown in Fig. 4(a) and Fig. S9 (in ESI). The corresponding line-cuts in the in-plane (IP) and out-of-plane (OOP) directions are shown in Fig. 4(b) and Fig. S10 (ESI), and the detailed parameters are listed in Table S6 (in ESI). The results show that the binary and ternary films exhibited a pronounced face-on orientation. The crystal coherence

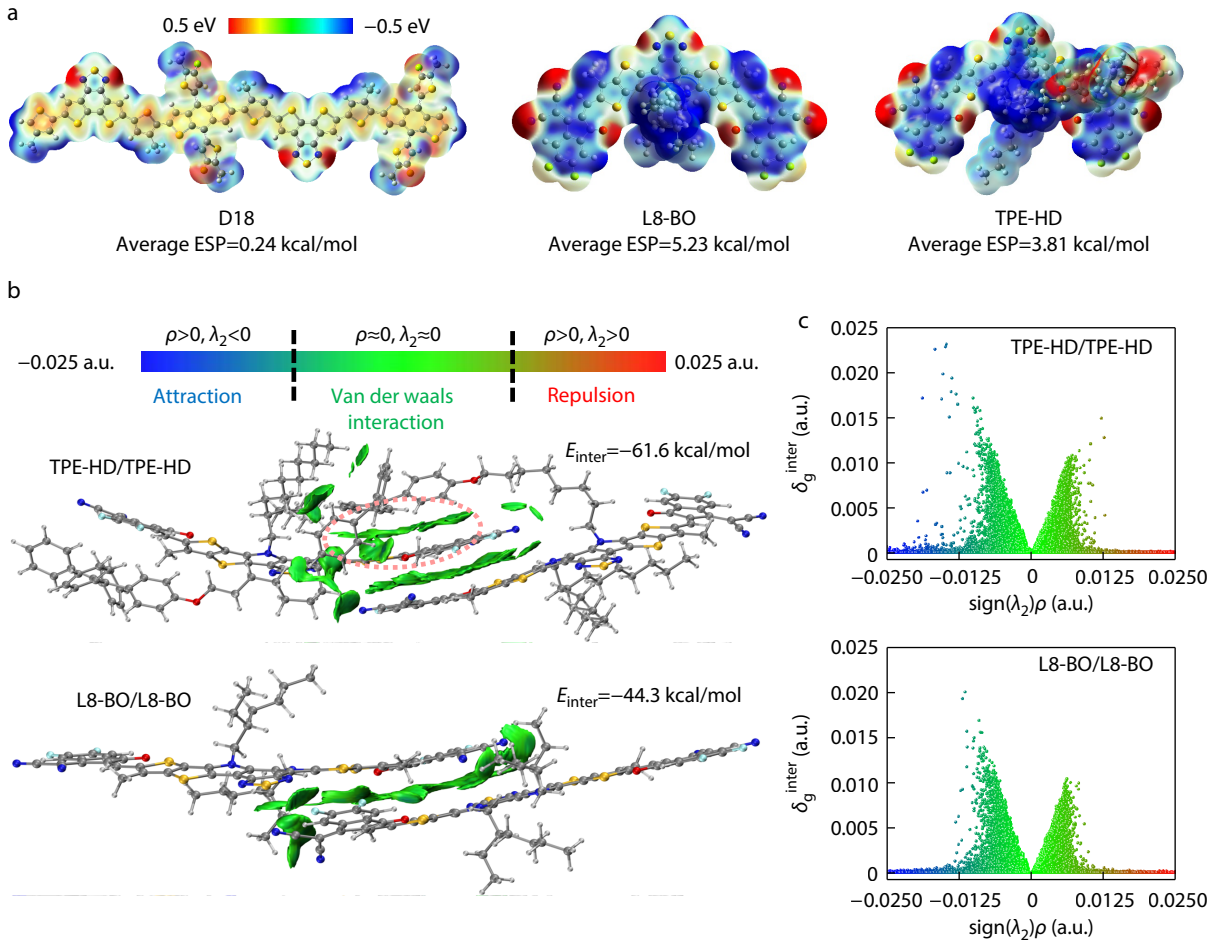

Fig. 3 (a) Surface electrostatic potential distribution of D18, L8-BO and TPE-HD; (b) The BSSE-corrected interaction energy and IGMH isosurfaces; (c) The IGMH scatter graphs of TPE-HD and L8-BO dimers.

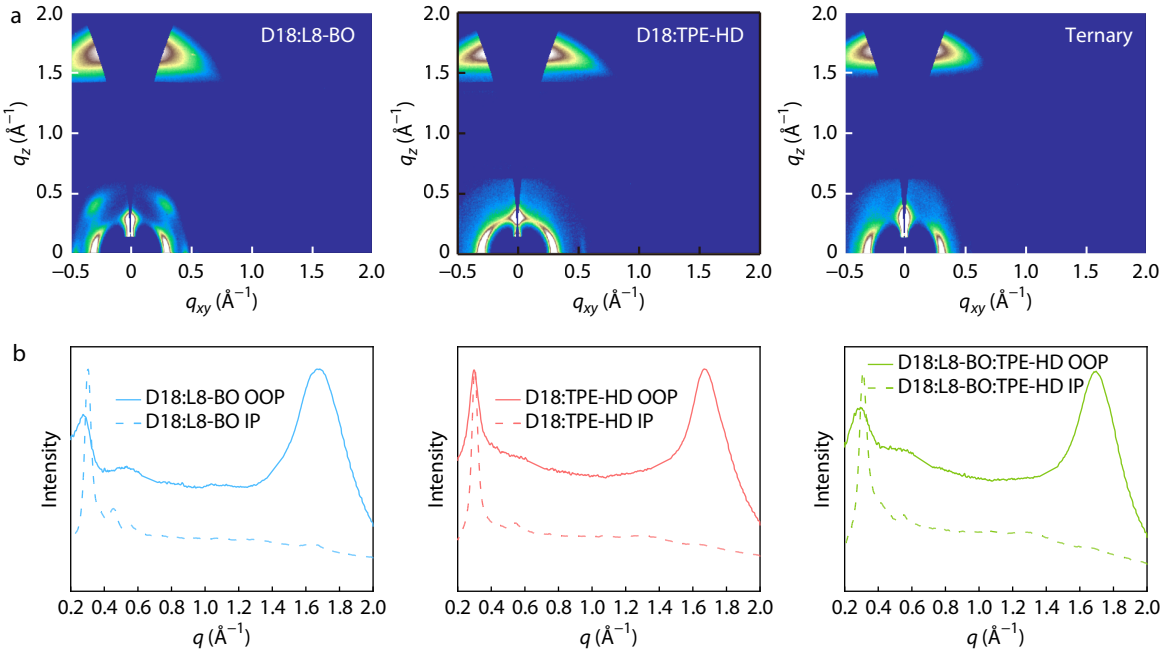

Fig. 4 (a) 2D GIWAXS patterns; (b) The corresponding GIWAXS 1D line-cuts of out-of-plane and in-plane directions.

https://doi.org/10.1007/s10118-026-3810-7

lengths (CCLs) along the (010) peak for the D18:L8-BO, D18:TPE-HD, and D18:L8-BO:TPE-HD blend films are calculated to be 22.20, 29.12, and 25.99 Å, respectively, among which the TPE binary blend film shows much higher crystallinity than D18:L8-BO. The GIWAXS results were consistent with the DFT calculations, confirming that the introduction of TPE-HD significantly enhanced the molecular packing.

To further understand the influence of the TPE unit on the film formation process, *in situ* UV-Vis absorption spectroscopy was performed during spin coating from chloroform, and the corresponding results are shown in Fig. 5. The evolution of the characteristic absorption peak of the film can generally be divided into three stages: solvent evaporation, solute precipitation and crystallization, and dry film formation. The second stage is the key stage characterizing the aggregation process, which is typically marked by a redshift in the acceptor absorption spectrum. The duration of the second stage for the D18:L8-BO, D18:L8-BO:TPE-HD, and D18:TPE-HD films was approximately 240, 180, and 160 ms, respectively, showing a progressively decreasing trend with increasing TPE-HD content. These results indicate that the incorporation of TPE-HD significantly accelerated nucleation and ordered molecular aggregation during film formation. This accelerated crystallization behavior can be attributed to the enhanced A/A interaction induced by the TPE-functionalized side chain, which increases the self-aggregation driving force and promotes molecular packing during solvent evaporation. Film-depth-dependent light absorption spectroscopy (FLAS) was used to probe the vertical phase distribution of the blend films (Fig. S11 in ESI). Excessive acceptor aggregation in the D18:TPE-HD film led to an imbalanced vertical D/A distribution, limiting exciton dissociation, whereas the strong donor–acceptor interaction in the D18:L8-BO film suppressed donor enrichment near the substrate, hindering hole collection. In contrast, the ternary blend simultaneously preserved sufficient D/A interfacial contact and an optimized vertical donor distribution, achieving a better balance between exciton dissociation and charge collection. These findings further demonstrate the role of TPE-HD in optimizing the blend morphology.

Combining intermolecular interaction analysis, morphology characterization, and film-formation kinetics, it is clear that the balance between D/A and A/A interactions governs the crystallization dynamics and blend morphology evolution. The enhanced A/A interaction induced by the TPE unit accelerated molecular aggregation during film formation, leading to faster crystallization and stronger molecular packing. However, in the D18:TPE-HD binary system, this results in excessive self-aggregation and pronounced phase separation, which are unfavorable for exciton dissociation. In contrast, introducing TPE-HD as a third component in the D18:L8-BO system moderated the D/A-A/A interaction balance, yielding optimized crystallization kinetics and a more favorable nanoscale morphology. As a result, the ternary blend enabled more efficient charge transport with reduced recombination loss, contributing to improved device performance.

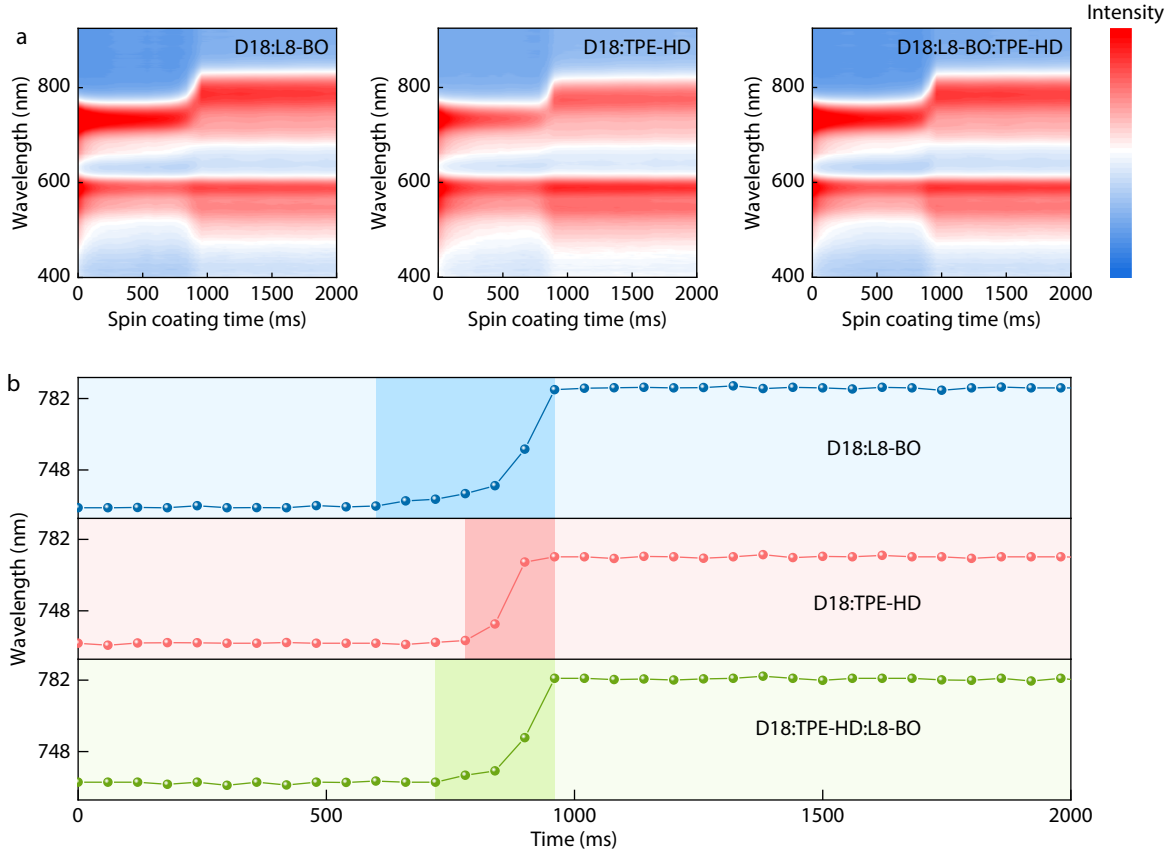

Fig. 5 (a) *In situ* 2D absorption contour maps; (b) Relevant time-dependent absorption peak shifts.

https://doi.org/10.1007/s10118-026-3810-7

CONCLUSIONS

In summary, a tetraphenylethylene-containing Y-series acceptor (TPE-HD) was synthesized through phenyl-alkyl side-chain engineering to regulate intermolecular interactions and aggregation. The introduced TPE side chains enhanced A/A self-aggregation and molecular ordering, leading to improved crystallinity and electron transport. TPE-HD was incorporated into the D18:L8-BO system as a third component to optimize the active-layer morphology and charge dynamics. Benefiting from the synergistic effects of efficient exciton generation from L8-BO and enhanced molecular packing induced by TPE-HD, the ternary blend exhibited more balanced phase separation, suppressed charge recombination, and improved charge transport. Consequently, the ternary organic solar cell achieved an outstanding PCE of 19.8%, accompanied by simultaneous enhancements in J_{SC}, FF, and V_{OC}. This work demonstrates that hybrid side-chain engineering is an effective strategy for modulating intermolecular interactions and highlights the great potential of ternary approaches for constructing high-performance organic solar cells through synergistic morphology optimization.

Conflict of Interests

The authors declare no interest conflict.

Electronic Supplementary Information

Electronic supplementary information (ESI) is available free of charge in the online version of this article at http://doi.org/10.1007/s10118-026-3810-7.

Data Availability Statement

The data supporting the findings of this study are available from the corresponding author upon reasonable request.

ACKNOWLEDGMENTS

This work was financially supported by the National Natural Science Foundation of China (No. 22475037) and the Anhui Provincial Natural Science Foundation (No. 2308085MA19). We would also like to express our gratitude to beamline BL02U2 at the Shanghai Synchrotron Radiation Facility (SSRF) for their support during the GIWAXS experiments.

REFERENCES

1 Yi, J.; Zhang, G.; Yu, H., Yan, H. Advantages, challenges and molecular design of different material types used in organic solar cells. *Nat. Rev. Mater.* **2024**, *9*, 46–62.
2 Meng, L.; Zhang, Y.; Wan, X.; Li, C.; Zhang, X.; Wang, Y.; Ke, X.; Xiao, Z.; Ding, L.; Xia, R.; Yip, H.-L.; Cao, Y., Chen, Y. Organic and solution-processed tandem solar cells with 17.3% efficiency. *Science* **2018**, *361*, 1094–1098.
3 Wang, Z.; Zhang, D.; Yang, L.; Allam, O.; Gao, Y.; Su, Y.; Xu, M.; Mo, S.; Wu, Q.; Wang, Z.; Liu, J.; He, J.; Li, R.; Jia, X.; Li, Z.; Yang, L.; Weber, M. D.; Yu, Y.; Zhang, X.; Marks, T. J.; Stingelin, N.; Kacher, J.; Jang, S. S.; Facchetti, A., Shao, M. Mechanically robust and stretchable organic solar cells plasticized by small-molecule acceptors. *Science* **2025**, *387*, 381–387.
4 Liu, C. H.; Lian, Y. C.; Song, J. L.; Duan, X. P.; Wang, Z., Sun, Y. M. A bisphosphonic acid-functionalized carbazole for dual hydrophilic interfaces toward efficient and stable organic solar cells. *Chinese J. Polym. Sci.* **2026**, *44*, 950–958.
5 Zhu, S.; Lyu, L.; Li, Y.; Li, W.; Cui, Y., Hu, H. Cyclization engineering of electron-deficient maleimide unit for nonfused ring electron acceptors enables efficient organic solar cells. *ACS Appl. Mater. Interfaces* **2024**, *16*, 33928–33934.
6 Ma, R.; Luo, Z.; Zhang, Y.; Zhan, L.; Jia, T.; Cheng, P.; Yan, C.; Fan, Q.; Liu, S.; Ye, L.; Zhang, G.; Xu, X.; Gao, W.; Wu, Y.; Wu, J.; Li, Y.; Liu, Y.; Liu, F.; Song, J.; Chen, H.; Chen, W.; Zhang, X.; Liu, Y.; Yuan, J.; Liu, Q.; Kan, Z.; Yin, H.; Li, X.; Ma, Y.; Deng, D.; Zhu, L.; Huo, Y.; Fan, B.; Fu, H.; Liao, X.; Hu, H.; Li, C.; Yu, R.; Hu, H.; Yao, Z.; Cai, Y.; Qian, D.; Cui, Y.; Yao, H.; Xu, B.; Kan, B.; Gao, K.; Duan, C.; Hu, X., Sun, H. Organic solar cells: beyond 20%. *Sci. China Mater.* **2025**, *68*, 1689–1701.
7 Fu, J.; Li, H.; Liu, H.; Huang, P.; Chen, H.; Fong, P. W. K.; Dela Peña, T. A.; Li, M.; Lu, X.; Cheng, P.; Xiao, Z.; Lu, S., Li, G. Two-step crystallization modulated through acenaphthene enabling 21% binary organic solar cells and 83.2% fill factor. *Nat. Energy* **2025**, *10*, 1251–1261.
8 Li, C.; Cai, Y.; Hu, P.; Liu, T.; Zhu, L.; Zeng, R.; Han, F.; Zhang, M.; Zhang, M.; Lv, J.; Ma, Y.; Han, D.; Zhang, M.; Lin, Q.; Xu, J.; Yu, N.; Qiao, J.; Wang, J.; Zhang, X.; Xia, J.; Tang, Z.; Ye, L.; Li, X.; Xu, Z.; Hao, X.; Peng, Q.; Liu, F.; Guo, L., Huang, H. Organic solar cells with 21% efficiency enabled by a hybrid interfacial layer with dual-component synergy. *Nat. Mater.* **2025**, *24*, 1626–1634.
9 Chen, L.; Liang, W.; Sergeev, A.; Lai, J. Y. L.; Zeng, X.; Wong, K. S.; Zhang, J.; Pun, S. H.; Yan, H., Hu, H. Benzannulation of furan: a strategy for stable and high-performance furan-containing giant electron acceptor with efficiency exceeding 20%. *Energy Environ. Sci.* **2025**, *18*, 6608–6617.
10 Liu, W.; Liang, W.; Zou, B.; Zhao, C.; Wang, F.; Zeng, P.; An, J.; Kong, Z.; Niu, J.; Chen, S.; Yan, H.; Wang, Y.; Zhang, G.; Zhang, J., Hu, H. Strategic inner/outer side-chain tuning for high-efficiency green-solvent-processed organic solar cells. *Sci. China Mater.* **2026**, *69*, 184–193.
11 Wang, Z.; Zhu, S.; Sun, K.; Guo, Y.; Zhao, Y.; Xiong, W.; Yu, M.; Zhang, G., Hu, H. Fluorination-controlled crystallization kinetics in donor polymers for 20% efficiency organic solar cells. *Adv. Funct. Mater.* **2026**, *36*, e30286.
12 Liang, W.; Zhu, S.; Sun, K.; Hai, J.; Cui, Y.; Gao, C.; Li, W.; Wu, Z.; Zhang, G., Hu, H. Achieving 19.72% efficiency in ternary organic solar cells through electrostatic potential-driven morphology control. *Adv. Funct. Mater.* **2025**, *35*, 2415499.
13 Xiong, W.; Cui, Y.; Zhang, Z.; Zhu, S.; Wang, Z.; Chai, Z.; Hu, H., Chen, Y. Manipulating σ-hole interactions in halogenated additives for high-performance organic solar cells with 19.8 % efficiency. *Angew. Chem. Int. Ed.* **2025**, *64*, e202500085.
14 Hu, K.; Ge, Y.; Yang, H.; Xu, Y.; Qian, J.; Zhu, X.; Wu, Y.; Cui, C., Li, Y. Dispersion effect of chlorination-induced intermolecular stacking optimization of small-molecule acceptors for high-performance organic solar cells. *Energy Environ. Sci.* **2025**, *18*, 9194–9204.
15 Zhang, W. P.; Liu, M. M.; Fu, M.R.; Gao, D.; Zhao, Q. Q.; Xiao, B., Zhao, T. X. "Bridging" structure polymer strategy for morphology regulation and performance optimization of organic solar cells based on the ternary-component polymer. *Chinese J. Polym. Sci.* **2026**, *44*, 813–820.
16 Wang, Z.; Zhu, S.; Peng, X.; Luo, S.; Liang, W.; Zhang, Z.; Dou, Y.; Zhang, G.; Chen, S.; Hu, H., Chen, Y. Regulating intermolecular interactions and film formation kinetics for record efficiency in

Graphical Abstract

Regulating Intermolecular Interactions through Phenyl-alkyl Side-chain Engineering for High-efficiency Organic Solar Cells

Yang Yi, Shen-Bo Zhu, Ming-Hao Jin, Jia-Yin Lyu, Zhi-Bo Wang, Rui-Han Li, Xiao-Nan Xu, Xue-Chen Jiao, and Hua-Wei Hu

Donghua University; University of Science and Technology of China

Through phenyl-alkyl side-chain engineering, a tetraphenylethylene-containing acceptor (TPE-HD) was developed to regulate intermolecular interactions, optimize film morphology and crystallization kinetics, enabling high-performance organic solar cells.

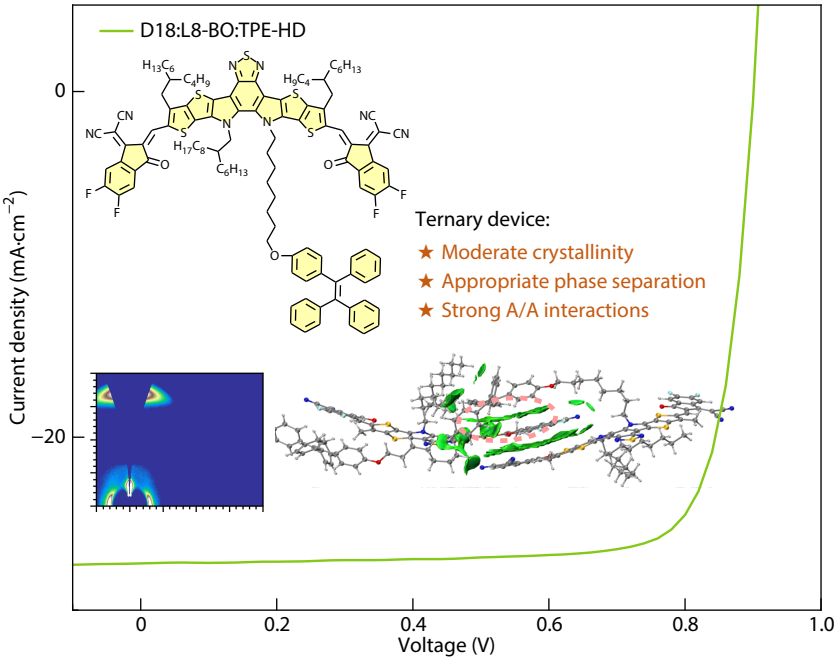

Chinese J. Polym. Sci., 2026 *https://doi.org/10.1007/s10118-026-3810-7*

difluorobenzothiadizole-based organic solar cells. *Angew. Chem. Int. Ed.* **2025**, *64*, e202412903.

17 Shang, A.; Luo, S.; Zhang, J.; Zhao, H.; Xia, X.; Pan, M.; Li, C.; Chen, Y.; Yi, J.; Lu, X.; Ma, W.; Yan, H., Hu, H. Over 18% binary organic solar cells enabled by isomerization of non-fullerene acceptors with alkylthiophene side chains. *Sci. China Chem.* **2022**, *65*, 1758−1766.

18 Zhu, L.; Zhang, Q. Z.; Ding, H.; Zhang, M.; Xue, X.N.; Zhong, W. K.; Zhou, Z. C.; Xu, J. Q.; Feng, W.; Zou, Y. C.; Zhang, Y. M., Liu, F. Unraveling the effect of solvent additive and fullerene component on morphological control in organic solar cells. *Chinese J. Polym. Sci.* **2022**, *40*, 1604−1612.

19 Yin, B.; Chen, Z.; Wu, B.; Yuan, X.; Xiao, C.; Zhou, X.; Zhong, J.; Lee, S.; Chen, W.; Zhang, L.; Wang, L.; Zhang, G.; Zhang, W.; Yang, C.; Liu, Z.; Huang, F.; Cao, Y., Duan, C. Chlorination-controlled aggregation and film-formation kinetics enabling high-efficiency organic solar cells with low-cost linear conjugated polymers. *Nat. Commun.* **2026**, *17*, 2340.

20 Liang, W.; Chen, L.; Wang, Z.; Peng, Z.; Zhu, L.; Kwok, C. H.; Yu, H.; Xiong, W.; Li, T.; Zhang, Z.; Wang, Y.; Liao, Y.; Zhang, G.; Hu, H., Chen, Y. Oligothiophene additive-assisted morphology control and recombination suppression enable high-performance organic solar cells. *Adv. Energy Mater.* **2024**, *14*, 2303661.

21 Lei, Y.; Meng, X.; Guo, Q.; Sun, X., Zhou, E. Recently progress of aromatic side chain engineering on Y6 for high performance organic solar cells. *Nano Res.* **2025**, *18*, 94907513.

22 Luo, Z.; Xu, T.; Zhang, C. e., Yang, C. Side-chain engineering of nonfullerene small-molecule acceptors for organic solar cells. *Energy Environ. Sci.* **2023**, *16*, 2732−2758.

23 Jiang, Y.; Sun, S.; Xu, R.; Liu, F.; Miao, X.; Ran, G.; Liu, K.; Yi, Y.; Zhang, W., Zhu, X. Non-fullerene acceptor with asymmetric structure and phenyl-substituted alkyl side chain for 20.2% efficiency organic solar cells. *Nat. Energy* **2024**, *9*, 975−986.

24 Mishra, A. Material perceptions and advances in molecular heteroacenes for organic solar cells. *Energy Environ. Sci.* **2020**, *13*, 4738−4793.

25 Ding, P.; Rong, X.; Yang, D.; Yu, X.; Shao, Z.; Wang, H.; Liao, X.; Cao, X.; Wu, J.; Xie, L.; Zhu, J.; Chen, F.; Chen, G.; Huang, Y., Ge, Z. Direct C–H arylation-derived low crystallinity guest acceptor for high efficiency organic solar cells. *Energy Environ. Sci.* **2025**, *18*,

6548−6556.
26 Li, K.; Xie, Q.; An, C.; Zhong, J.; Yao, Y.; Hong, C.; Chen, Y.; Geng, H.; Wu, Y.; Zhang, W.; Liao, Q., Fu, H. A nonfused ring electron acceptor with aggregation-induced emission assistance achieving over 20% efficiency in organic solar cells. *Angew. Chem. Int. Ed.* **2025**, *64*, e202506415.
27 Zhou, X.; Liang, W.; Ma, R.; Zhang, C.; Peng, Z.; Dela Peña, T. A.; Wu, J.; Ma, Z.; Liao, Y.; Li, G., Hu, H. Synergistic control of multilength-scale morphology and vertical phase separation for high-efficiency organic solar cells. *Energy Environ. Sci.* **2024**, *17*, 7762−7771.
28 Li, L.; Xiong, W.; Zhang, Y.; Wang, Z.; Dong, J.; Zhu, S.; Li, X.; Hu, M.; Wu, J.; Hu, H., Hai, J. Unsaturated vinyl branching: a molecular-tailoring strategy for synergistic stacking regulation and energy-loss suppression toward 20%-efficiency organic solar cells. *Adv. Mater.* **2026**, *38*, e20692.
29 Jeon, S. J.; Yang, N. G.; Kim, J. Y.; Cho, E.; Park, J.; Lee, G.; Yang, C., Moon, D. K. Streamlined Y6-analogs enabling efficient ambient-air-processed organic solar cells. *Adv. Energy Mater.* **2026**, *16*, e05110.
30 Qiao, C. Y.; Xie, Q.; Fang, J.; Xia, D. D.; Zhang, Y. F.; Wang, J. L.; You, S. Y.; Jiang, L.; Huang, B.; Li, W. W.; Zhao, C. W., Xie, Y. Asymmetric alkyl chain engineering of non-fullerene acceptors for efficient organic solar cells. *Chinese J. Polym. Sci.* **2025**, *43*, 994−1000.
31 Oh, S.; Bae, K.; Jeong, D.; Phan, T. N.-L.; Lee, J.-W., Kim, B. J. Dual side chain functionalization of small molecule acceptors affords high-performance organic solar cells with refined blend morphology. *Adv. Funct. Mater.* **2025**, *35*, 2502707.
32 Wang, P.; Bi, F.; Li, Y.; Han, C.; Zheng, N.; Zhang, S.; Wang, J.; Wu, Y., Bao, X. Manipulating the intermolecular interactions through side chain engineering and unilateral π-bridge strategy for efficient small molecular photovoltaic acceptor. *Adv. Funct. Mater.* **2022**, *32*, 2200166.
33 Song, H.; Yue, Y.; Gui, X.; Sun, S.; Yang, Z.; Zheng, B.; Shen, H.; Wang, J.; Zhang, J., Huo, L. Strategic engineering of H-/J-aggregation equilibrium in non-fullerene acceptors toward high-performance organic photovoltaics. *Energy Environ. Sci.* **2026**, *19*, 1703−1714.
34 Li, Z.; Ding, X.; Jiang, D.; Ding, Y.-F.; Liu, B.; Zhao, Y.-Q.; Zeng, D., Yin, H. Regulating polymeric adsorption dynamics *via* monolayer-architected hydrotalcite integration for high-performance organic solar cells. *Adv. Mater.* **2025**, *37*, 2508049.
35 Liu, J.; Cai, W.; Yin, Y.; Wang, M.; Zhang, J.; Qamar, S.; Zheng, X.; Guo, H.; Liu, N.; Li, S.; Bian, J.; Shi, Y., Cai, W. Enhanced performance of perovskite solar cells *via* multifunctional carbon quantum dot modification. *Energy Mater. Adv.* **2025**, *6*, 0197.
36 Liu, N.; Xu, F.; Jing, J.; Shi, J.; Song, T.; Zhou, H.; Bai, Y.; Jiang, Y.; Du, M.; Chen, L.; Kulakovich, O.; Li, S.; Chang, S.; Zhu, C., Chen, Q. Amidinium-enhanced charge dissociation in homogeneous quasi-2-dimensional perovskite solar cells. *Energy Mater. Adv.* **2025**, *6*, 0187.
37 Zhu, S.; Cui, Y.; Xiong, W.; Zhang, C.; Jiang, Y.; Liu, F.; Shi, X.; Ma, Z.; Zhu, X.; Liao, Y., Hu, H. Electronegativity-engineered multidimensional interactions enable 20% efficiency organic solar cells. *Adv. Energy Mater.* **2025**, *15*, 2502643.
38 Zhang, K.; Guo, M.; Shi, Y.; Wang, L.; Han, P.; Zhang, Y.; Li, S.; Song, P., Li, Y. Natural photosensitizer for regulating organic solar cells: coupling mechanisms of intermolecular interactions and energy-charge transfer. *J. Phys. Chem. Lett.* **2026**, *17*, 493−510.
39 Hu, H.; Liu, S.; Xu, J.; Ma, R.; Peng, Z.; Peña, T. A. D.; Cui, Y.; Liang, W.; Zhou, X.; Luo, S.; Yu, H.; Li, M.; Wu, J.; Chen, S.; Li, G., Chen, Y. Over 19 % efficiency organic solar cells enabled by manipulating the intermolecular interactions through side chain fluorine functionalization. *Angew. Chem. Int. Ed.* **2024**, *63*, e202400086.
40 Zhou, J.; Xiong, W.; Chai, Z.; Gu, D.; Xu, Y.; Wang, Z.; Zhu, S.; Cui, Y., Hu, H. Regulating molecular packing and crystallization kinetics *via* trifluoromethyl-functionalized solid additives for efficient organic solar cells. *J. Mater. Chem. A* **2026**, *14*, 24580−24588.
41 Lu, T., Chen, Q. Independent gradient model based on Hirshfeld partition: a new method for visual study of interactions in chemical systems. *J. Comput. Chem.* **2022**, *43*, 539−555.
42 Lu, T., Chen, F. Multiwfn: a multifunctional wavefunction analyzer. *J. Comput. Chem.* **2012**, *33*, 580−592.